Fluid transport in shale gas reservoirs

Elsevier Editorial System(tm) for
International Journal of Coal Geology
Manuscript Draft

Manuscript Number: COGEL-D-15-00606R1

Title: Fluid Transport in Shale Gas Reservoirs: Simultaneous Effects of Stress and Slippage on Matrix Permeability

Article Type: Research Paper

Keywords: Shale permeability; Slip flow; Geomechanical effect; Gas permeability prediction

Corresponding Author: Mr. Rasoul Nazari Moghaddam,

Corresponding Author's Institution: Heriot Watt University

First Author: Rasoul Nazari Moghaddam

Order of Authors: Rasoul Nazari Moghaddam; Mahmoud Jamiolahmady, Professor

Abstract: Gas flow modelling in shale and tight gas reservoirs is challenging mainly due to different pore-scale flow regimes present in micro- and nanopores of these reservoirs. The effect of geomechanical stress also significantly affect the measurement and prediction of apparent matrix permeability. In this study, series of experiments were designed and performed on three shale samples to study the simultaneous effects of slippage and stress at five different pore pressures and four net stresses. The experimental data were used to obtain a general slip plot, which quantifies the effects of slippage on matrix permeability. Then, the stress effects were taken into account by modifying the average pore size and non-slip permeability at each net stress based on the experimental observations. It is found that the non-slip permeability of matrix and average pore size follow an exponential behaviour when changing the net stress. These two relationships were then incorporated into the corresponding slip flow model in order to capture the effects of slippage and stress at the same time. The validity of the proposed model was also investigated (using published data in the literature) which shows that the proposed technique is able to capture the intensity of permeability reduction and enhancement due to stress and slippage, respectively. This study increases our knowledge of rarefied flow dynamic inside micro- and nano-pores under confining stress, which is necessary for accurate prediction of apparent matrix permeability in the unconventional reservoirs.

Suggested Reviewers:

Opposed Reviewers:

Response to Reviewers: Dear Editor:
I would like to resubmit the revised version of Manuscript # COGEL-D-15-00606 “Fluid Transport in Shale Gas Reservoirs: Simultaneous Effects of Stress and Slippage on Matrix Permeability”. We appreciate the time and efforts spent by the editor and referees in reviewing this manuscript. The comments were constructive and accordingly we have addressed them.

Please see below details of our responses to each of these comments. It should be mentioned that, in the revised version, full characterisation of the samples including TOC and minerology (XRD results) have been added.

Kind Regards,
Rasoul Nazari Moghaddam

Fluid Transport in Shale Gas Reservoirs: Simultaneous Effects of Stress and Slippage on Matrix Permeability

Rasoul Nazari Moghaddam, Mahmoud Jamiolahmady
Institute of Petroleum Engineering, Heriot Watt University

Abstract

Gas flow modelling in shale and tight gas reservoirs is challenging mainly due to different pore-scale flow regimes present in micro- and nanopores of these reservoirs. The effect of geomechanical stress also significantly affect the measurement and prediction of apparent matrix permeability. In this study, series of experiments were designed and performed on three shale samples to study the simultaneous effects of slippage and stress at five different pore pressures and four net stresses. The experimental data were used to obtain a general slip plot, which quantifies the effects of slippage on matrix permeability. Then, the stress effects were taken into account by modifying the average pore size and non-slip permeability at each net stress based on the experimental observations. It is found that the non-slip permeability of matrix and average pore size follow an exponential behaviour when changing the net stress. These two relationships were then incorporated into the corresponding slip flow model in order to capture the effects of slippage and stress at the same time. The validity of the proposed model was also investigated (using published data in the literature) which shows that the proposed technique is able to capture the intensity of permeability reduction and enhancement due to stress and slippage, respectively. This study increases our knowledge of rarefied flow dynamic inside micro- and nano-pores under confining stress, which is necessary for accurate prediction of apparent matrix permeability in the unconventional reservoirs.

1. Introduction

Decline in gas production from conventional resources and advances in technology have increased the important role of the Unconventional Gas Resources (UGRs) in the global gas production. The main characteristic of the unconventional reservoirs is low matrix permeability that makes the dynamics of fluids flow and their interaction with surfaces to be very different from those in conventional systems.

Gas production in shale reservoirs is attributed to the conductivity of the matrix and fracture systems. However, the long term gas production from these reservoirs are known to be a

function of fluid transport in the matrix (Bustin and Bustin, 2012; Swami and Settari, 2012). Many researchers have shown the importance of the matrix flow (Bustin and Bustin, 2012; Bustin et al., 2008; Kalantari-Dahaghi, 2011) and several theoretical models have been published mainly to predict the matrix apparent permeability (Civan, 2010; Darabi et al., 2012; Deng et al., 2014; Fathi and Akkutlu, 2013; Florence et al., 2007; Freeman et al., 2011; Javadpour, 2009; Kazemi and Takbiri-Borujeni, 2015).

The shale gas permeability measurement is challenging mainly due to simultaneous presence of different processes such as rarefaction flow, gas adsorption/desorption, and geo-mechanical effects. The rarefaction term refers to conditions, whereby the gas phase becomes less dense or the gas particles more spread out. At such conditions, the mean free path (MFP) of gas molecules becomes significant relative to the dimensions of the flow conduit. As a result, the impact of the Knudsen layer on the overall flow performance increases. Knudsen layer is an area near the wall surface with an approximate thickness of ~O(λ) where the momentum diffusivity of the gas is significantly changed due to the presence of solid boundary. In the Knudsen layer, the N-S equations are not able to capture the flow behaviour as the assumptions of N-S equations (continuum hypothesis) are no longer valid.

A key dimensionless parameter for considering the rarefaction effect is the Knudsen number, which is defined as the ratio of the mean free path (λ) over the flow conduit characteristic length (L). The rarefaction effect increases as the Knudsen number increases. Similar to gas flow at low pressure, which experiences the rarefaction (due to an increase in the mean free path), the flow at micro- and nano-system can experiences rarefied flow due to reduction in the characteristic length.

In addition to the rarefied flow in the matrix, geo-mechanical effects or stress-dependent permeability is another active phenomenon, which should be considered, when investigating the gas flow in shale matrices. In other words, shale matrix permeability is highly stress-dependent (Gutierrez et al., 2014; Gutierrez et al., 2000; Jones and Owens, 1980). It is believed that the opening and closure of finely-distributed pore throats between the clay minerals are responsible for strong stress-dependency of shale permeability (Dewhurst and Siggins, 2006; Gutierrez et al., 2014). In the past, it has been reported that the stress dependent permeability of non-shale rocks can be described by an exponential relationship (Brace et al., 1968; Evans et al., 1997; Schmoker and Halley, 1982). In addition, it is reported in the literature that permeability and porosity is not only dependent on the stress, but also on

the history of loading and unloading stresses. Hence hysteresis is observed when measuring stress dependent permeability (Kwon et al., 2004).

There are several theoretical works on permeability modelling (Civan, 2010; Deng et al., 2014; Florence et al., 2007; Freeman et al., 2011; Javadpour, 2009; Kazemi and Takbiri-Borujeni, 2015), of systems with micro and nano-pores but there are few reported studies, which investigate the dominant mechanisms experimentally. Ghanizadeh et al. (2014) conducted a laboratory study examining the transport properties in the matrix of the Lower Toarcian Posidonia Shale. The main objective of their case study was to provide high-quality experimental data, when analysing the effects of different parameters (Ghanizadeh et al., 2014a). Firouzi et al. (2015) conducted pressure pulse decay experiments and measured the helium permeability and Klinkenberg parameters of a shale core plug. They compared the measured permeabilities and the permeability predictions using non-equilibrium Molecular Dynamics (MD) simulations indicating that the pulse-decay gas permeability is approximately two orders of magnitude greater than that calculated by the MD simulations (Firouzi et al., 2014). Guo et al. (2015) presented an experimental study of nitrogen flow through nano membranes. They also proposed a new mathematical model to characterize gas flow in such nano pores. In addition, they derived a new apparent permeability expression based on viscous flow and Knudsen diffusion. Ghanizadeh et al. (2015) conducted some experiments to characterize the porosity, pore size distribution and permeability of Montney and Bakken shale formations in Canada.

In addition, there are recent experimental works, which study the stress dependency of the shale permeability. Dong et al. (2010) measured the stress dependent permeability and porosity of fine-grained sandstones and a silty-shale. They showed that the dependency of gas permeability to the stress can be better expressed using a power law function (Dong et al., 2010). Chalmers et al. (2012) conducted some experiments to investigate the geological parameters controlling the matrix permeability of Devonian shales. They reported that permeability is a function of mineral distribution, pore size, and fabric. Gut et al. (2014) investigated the use of the Constant Rate of Strain (CRS) consolidation test for measurements of continuous stress-dependent permeability, compressibility and poroelasticity of stiff and low-permeability shales.

As noted above, there are several independent experimental works on stress dependent permeability and rarefaction flow. However to the best of our knowledge, there is no experimental work studying the combined effect of the rarefied gas dynamics and geomechanical effects.

In this paper, results of series of experiments performed on three shale samples to investigate the slippage and geomechanical effects on matrix permeability, are reported. Steady state and unsteady state techniques were used to measure the gas permeability. The apparent permeabilities were measured at five different pore pressures and four net stresses. The conducted mercury injection capillary pressure (MICP) tests were used to characterize the pore size distribution of the shale samples. Knudsen numbers were calculated in each experiments based on the calculated mean free path of the flowing gas and an average pore size. The impacts of net stress on permeability were quantified based on the calculated Knudsen number and modified average pore size in each experiment.

Based on the results, the apparent matrix permeability can be better predicted considering both slippage and geomechanical effects using the proposed technique for modifying the average pore size, non-slip permeability and slip coefficients.

2. Experiments: material and methods

The experiments were performed on three shale rock samples (Eagle ford, Pierre and Barnett) using nitrogen gas. For hydrocarbon bearing rocks such as coal and shale, nitrogen and helium are commonly used and believed to have minimal effects on permeability measurements due to adsorption (Cui et al., 2009). The basic properties of shale samples are summarized in Table 1. All experiments were performed at constant temperature of 60 ℃ inside an oven. The temperature fluctuation inside the oven was recorded for 24 hours, which showed $\pm$0.1 ℃ variation. Prior to any experiment, a gas leakage test at high temperature was performed. All rock samples were cut parallel to beddings. To remove the initial water, all rock samples were dried at 105 ℃ overnight, while connected to the vacuum pump. The accuracy of the pressure transducers is ±0.015% FS and accurate quizix pumps are used for displacement and applying the overburden pressure. It is believed that the stress equilibrium in such rocks is a slow viscoelastic dominated process. Thus adequate time is required to reach the equilibrium after each change. In this study, to reach the equilibrium, the permeability was measured 24 hours after changing the overburden and pore pressure. The dead volume of all lines and valves were measured based on the Boyle two cell method using nitrogen at low pressure. In addition, minerology of shale samples were determined by whole-rock x-ray diffraction (XRD) analyses. Table 2 presents the minerology of three shale samples used in this study.

Table 1

Basic properties of the three shale rock samples used in this study.

Shale Sample	Length (cm)	Diameter (cm)	Porosity (%)	TOC (%)	Permeability Range (D)	Moisture Condition	Orientation wrt bedding
Eagle Ford	4.61	3.81	13.4	3.28	$\sim 10^{-4}$	Fully Dry	Parallel to bedding
Pierre	2.54	3.81	31.6	0.50	$\sim 10^{-5}$	Fully Dry	Parallel to bedding
Barnett	2.55	3.81	8.60	11.40	$\sim 10^{-6}$	Fully Dry	Parallel to bedding

Table 2

Minerology of the three shale samples, used in this study, obtained from whole-rock x-ray diffraction (XRD) analyses.

Shale Sample	Silicates			Carbonates			Phyllosilicates/Clay minerals				Others		
	Quarts	Plagioclase	K-feldspar	Calcite	Dolomite	Siderite	Mica*	Kaolinite	Chlorite	Smectite	Pyrite	Fluorapatite	Gypsum
Eagle Ford	27.1	nd**	<0.5	68.4	nd	nd	1.0	1.6	nd	nd	<0.5	nd	1.2
Pierre	68.3	2.1	nd	0.6	nd	nd	15.9	<0.5	2.2	10.3	0.7	nd	nd
Barnett	55.3	nd	nd	nd	nd	1.1	32.0	1.0	2.0	nd	0.8	7.8	nd

* Undifferentiated mica species possibly including muscovite, biotite, illite, illite/smectite.

** Not detected

Knudsen numbers were calculated for each experiment considering each pore pressure and net stress. For calculation of Knudsen numbers, it was assumed that one average flow "characteristic length" value could be allocated to each rock. For this purpose, the conducted ultrahigh pressure MICP experiments on core trim samples were used to determine the pore size distributions. Figs. 1 and 2 show the capillary pressure and pore size distributions of the

rock samples. For average pore size estimation, the measured pore sizes were fitted by appropriate well-known probability distribution functions that were subsequently used to characterise the rocks. These fitted probability functions cover all pore sizes, it can be presumed that the smaller pores, which were not saturated during the MICP test, (particularly those of the Barnett sample) have also been taken into account to some extent. As shown in Fig. 2, for Eagle Ford and Pierre, a normal distribution function is the best probability function to describe the pore sizes. For Barnett, a Gamma distribution function is identified as the best probability function of the pore sizes. Table 3 shows the statistical parameters of the pore size distributions. The mean pore size of shale samples was used as an average flow conduit characteristic length for the Knudsen number calculations in each experiment at the net stress of 500 psi. At higher net stress values, and as described later in this work, the mean pore size was modified to present an appropriate characteristic length for the system, based on the best match to the plot of the dimensionless permeability enhancement versus Knudsen number.

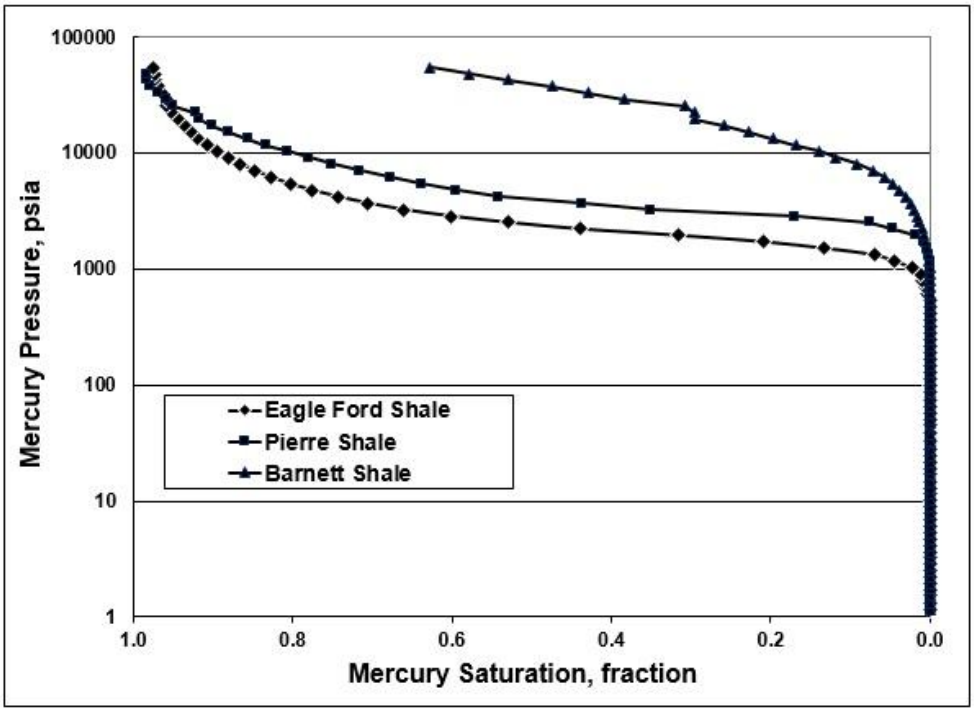

Fig. 1. MICP capillary pressure of (a) Eagle Ford (b) Pierre and (c) Barnett rock samples.

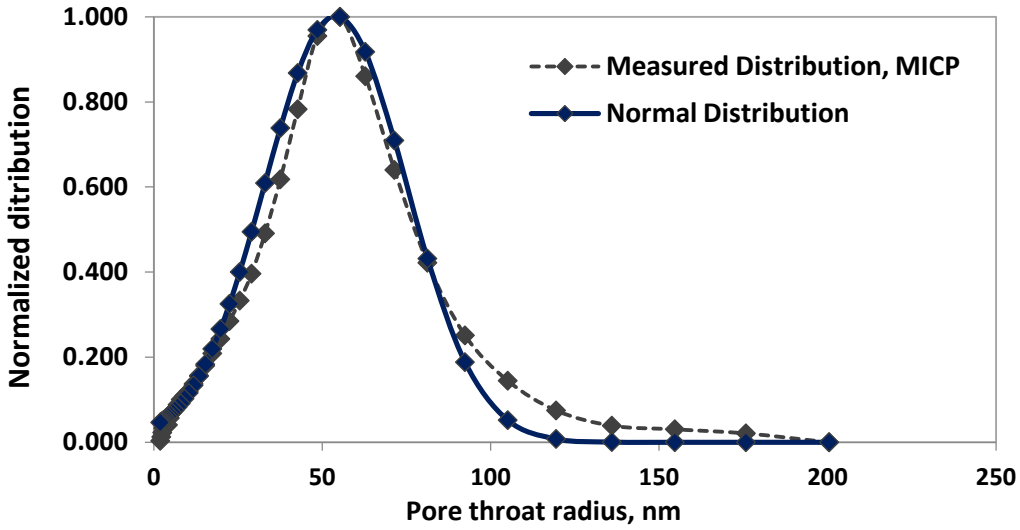
Normalized ditribution
1.000
0.800
0.600
0.400
0.200
0.000
0
50
100
150
200
250
Pore throat radius, nm
Measured Distribution, MICP
Normal Distribution

(a)

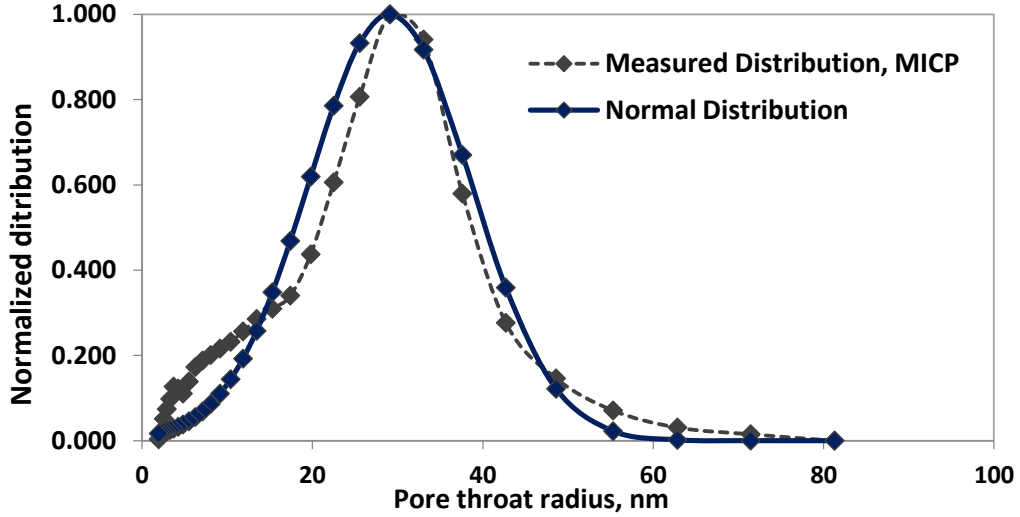
Normalized ditribution
1.000
0.800
0.600
0.400
0.200
0.000
0
20
40
60
80
100
Pore throat radius, nm
Measured Distribution, MICP
Normal Distribution

(b)

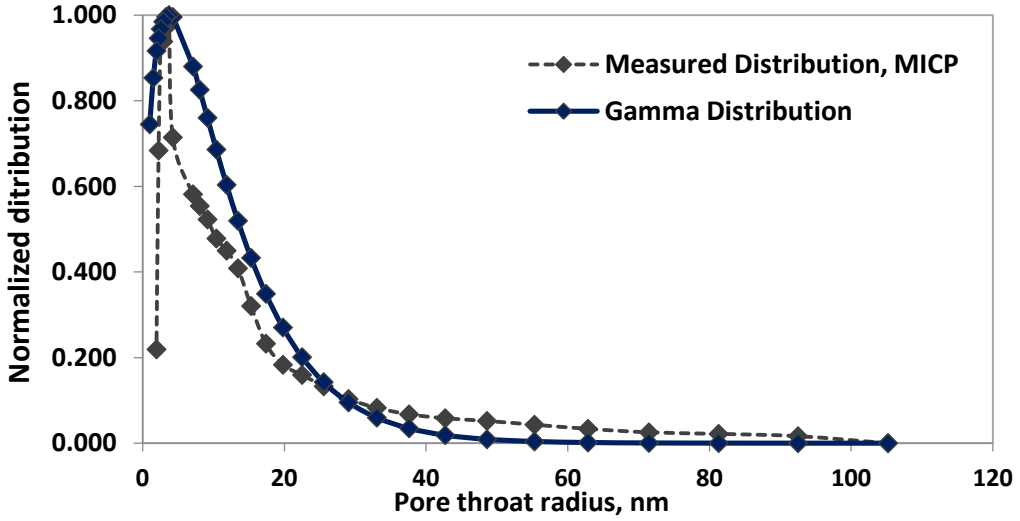
Normalized ditribution
1.000
0.800
0.600
0.400
0.200
0.000
0
20
40
60
80
100
120
Pore throat radius, nm
Measured Distribution, MICP
Gamma Distribution

(c)

Fig. 2. Pore size distribution of (a) Eagle Ford (b) Pierre and (c) Barnett rock samples. The best identified probability function is also shown for each sample.

Table 3

Pore size statistical parameters of three shale rock samples based on the measured MICP pore size distribution and best fitted probability function.

Shale sample	Probability function	Mean (μ)	Standard Deviation (σ)
Eagle Ford	Normal	54 nm	21 nm
Pierre	Normal	29.1 nm	9.5 nm
Barnett	Gamma	11.25 nm	9.2 nm

In addition to measured pore size distribution by MICP for all shale samples, void spaces and pore structure of the Eagle ford shale matrix were studied by Scanning Electron Microscopy (SEM). Pore types in shale and mudrocks are classified into two main groups of nonorganic-matter-related pores (interparticle, intraparticle and intracrystalline) and organic-matter-related pores (Jennings et al., 2013; Loucks et al., 2010). Micro-fractures are also classified among the effective pores, which have significant impact on storage and flow capacity. It is noted that these micro-fractures could be the artefacts of post-coring stress release or sample preparation. However, naturally occurring micro-fractures are also frequently observed in shale and mud rocks (Chalmers et al., 2012a; Jennings et al., 2013; Kwon et al., 2004; Wu et al., 2015) with significant contribution to the flow (Wu et al., 2015).

Fig. 3 shows that micro-fractures (MF) observed in the Eagle ford shale matrix. In addition to these microfractures, other pore types including interparticle and intraparticle pores are also observed. Fig. 4 presents more details about the available pores. These micro-fractures are mostly generated parallel to bedding (Kwon et al., 2004). In Fig. 4(a) a micro-fracture is illustrated with an approximate length of 60 μm. Interparticle (IP) pores are shown by yellow arrows in Fig. 4(b). Interparticle pores can be found between grains and crystals, which are generally related to the primary pore network. Interparticle pores are the most common pore type found in the Eagle ford (Jennings et al., 2013). In Fig. 4(c), intraparticle (IT) pores are shown by green arrows. Intraparticle pores are generally defined as the pores within a particle

boundary, which can be primary (original pores within grains that are clustered together such as pores within framboidal pyrite as shown in Fig. 3(c)) or secondary (dissolution pores) in origin. It is noted that these pore types are more common and can be easily detected. Despite different pore types observed in the structure of Eagle ford, it is believed that the micro-fractures have dominant contributions in both flow and stress-dependency behaviour of such shale formations. It seems that the micro-fractures observed on Eagle Ford SEM images are naturally occurring. Presence of framboidal pyrite and finer sediments inside a micro-fractures (shown Fig. 4(c)), decreases the possibility of fracture propagation during the core preparation. In addition, no macro-fractures were detected on these pictures.

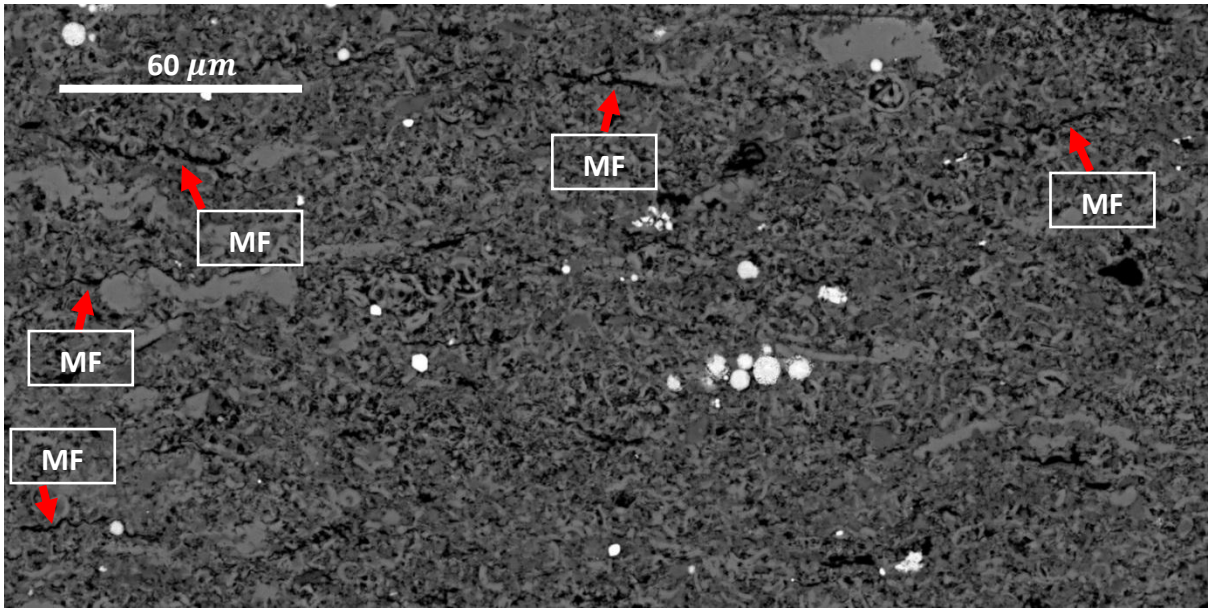

Fig. 3. SEM image of Eagle Ford shale sample which shows the interparticle microfractures (MF) by red arrows.

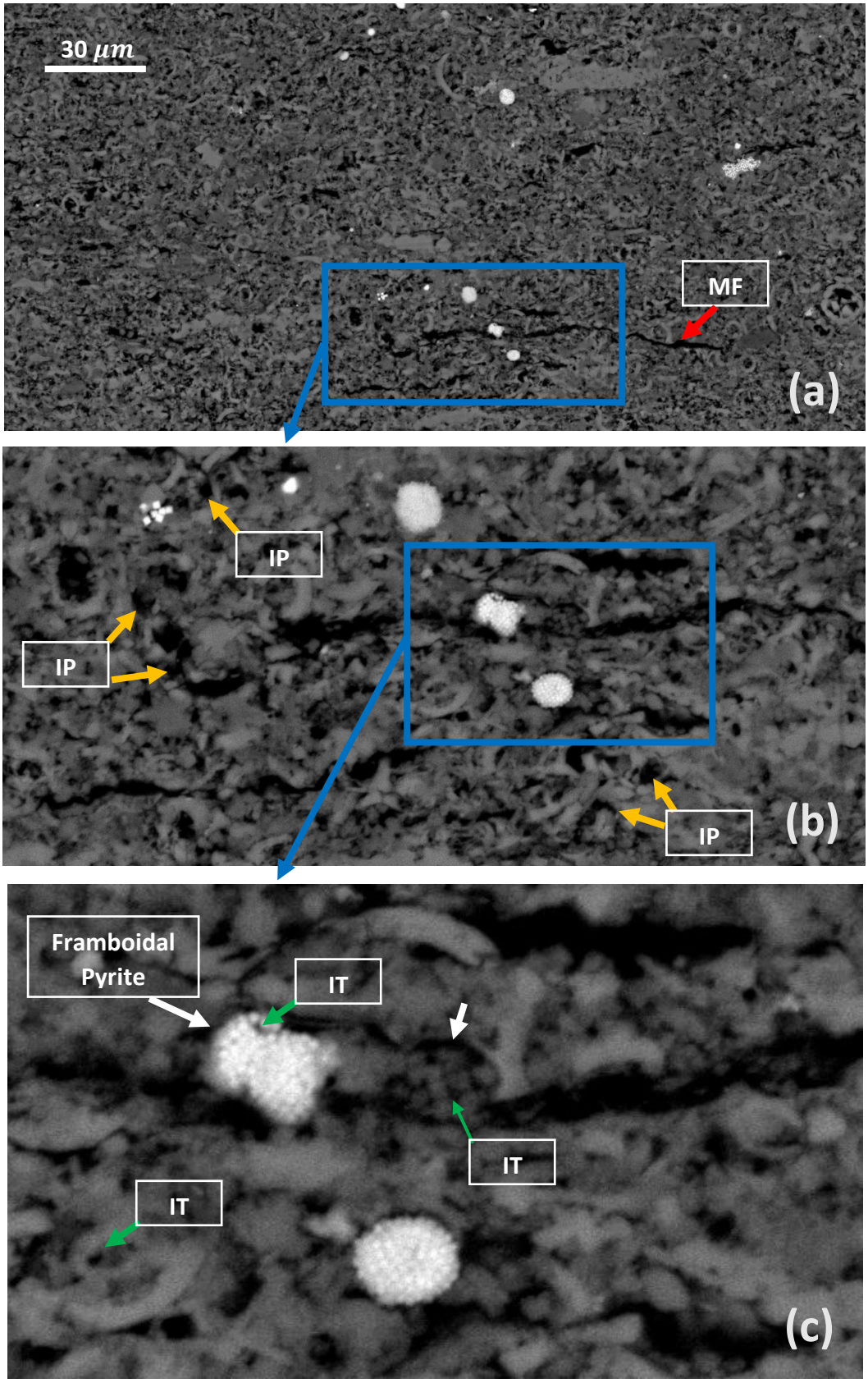

Fig. 4. Different pore types observed on SEM image of Eagle Ford shale. Presence of framboidal pyrite and finer sediments inside a micro-fracture (shown by white arrows) decreases the possibility of fracture propagation during the core preparation.

For experimental measurements in this work, pore pressures were designed in such a way to study rarefied flow, when the Knudsen numbers were between 0.01 and 1. Flow regimes are classified in Table 4 based on dimensionless Knudsen number. Based on this classification, the current experiments are within the slip flow regime and small part of the transition regime. There are several theoretical studies investigating all flow regimes in shale reservoirs including the free-molecule regimes (Darabi et al., 2012; Deng et al., 2014; Javadpour, 2009). However recent experimental observations have shown that gas mostly encounters the slip flow and transition flow in shale and tight gas reservoirs (Ghanizadeh et al., 2014b; Heller et al., 2014; Sinha et al., 2013; Yves et al., 2015) and rarely experiences free-molecular flow.

The main aim of this study is to accurately predict matrix permeability, when gas slippage and geo-mechanical effects are dominant. For matrix permeability measurements, steady state (for Eagle Ford) and unsteady state techniques (for Pierre and Barnett) were used. A schematic diagram of the steady state and unsteady state (pulse-decay) apparatus are shown in Fig. 5.

In order to calculate the Knudsen number for each experiment λ is calculated based on the following equation:

$$\lambda = \frac{k_B T}{\sqrt{2}\,\pi\sigma^2 P} \tag{1}$$

where k_B is the Boltzmann constant (1.3805×10^{-23} J/K), T is the absolute temperature, P is the gas pressure, σ is the collision dimeter of gas molecule. Collision diameter can also be estimated from gas viscosity using the following equation (Hildebrand, 1976) :

$$\sigma^2 = \frac{2\sqrt{m k_B T}}{3\,\pi^{3/2}\mu} \tag{2}$$

where m is the molecule mass and μ is the gas viscosity. All fluid parameters, e.g. gas viscosity, were extracted from the NIST data base (NIST, 2015). The analytical solution of the diffusivity equation for pulse-decay experiments was used to determine rocks permeability (Bourbie and Walls, 1982; Brace et al., 1968; Chen and Stagg, 1984; Dicker and Smits, 1988; Hsieh et al., 1981; Jones, 1997). As recommended by Jones (Jones, 1997) equal upstream and downstream reservoir volumes were used to produce the desirable effects of maintaining a constant mean pore pressure, which would ensure constant average fluid viscosity and compressibility. Darabi et al. (2012) have shown that, the variations of μ and C_g with pressure across the core have a negligible effect on the solution of the unsteady state

method (Darabi et al., 2012). In addition, the reliability of the unsteady state pulse decay method was examined by performing both unsteady and steady state tests on an Eagle Ford rock sample. The results showed ± 2 % difference between steady state and unsteady state measurements. In the unsteady-state experiments, upstream and downstream cell volumes were equal to 40 cc. The pressure difference between two upstream and downstream cells at the beginning of the experiments was less than 10% of the average pressure. Table 5 shows the density differences across the Eagle Ford rock sample for the highest pressure drop in each test. Based on these data, the flow can be assumed incompressible. The Reynold and Mach numbers were also calculated at each test as presented in Table 5. The calculated Reynolds and Mach numbers justify the assumptions used in this paper to simplify the NS equations.

In all permeability measurements, experiments were started from the highest pore pressure of 3000 Psi and completed at the lowest pore pressure of 250 Psi. The overburden pressure was also decreased step by step to obtain the desired net effective stress (difference in overburden and pore pressure). As the net stress effect is believed to be irreversible to great extent, the experiments were started from a low net stress of 500 and completed at the highest net stress of 3000 with two intermediate steps of 1000 and 2000 psi. This trend is also in agreement with what happens in reservoirs during their production life.

Table 4

Flow regimes classification for rarefied gas flow(Zhang et al., 2012).

Flow Regime	Description
Continuum Flow	$Kn < 10^{-2}$; The continuum and thermodynamic equilibrium assumptions are valid, and the flow can be described by N–S equations with conventional no-slip boundary conditions
Slip Flow	$10^{-2} < Kn < 10^{-1}$; The non-equilibrium effects dominate near the walls but continuum assumption within the fluid bulk is valid. The slip boundary models can be applied to N–S equations to describe the rarefaction effects of this flow regime.
Transition Flow	$10^{-1} < Kn < 10$; The rarefaction effects are dominated and the stress-strain relationship for the gas flow becomes nonlinear near the Knudsen layer (Barber and Emerson, 2006).
Free-molecular Flow	$Kn > 10$; Non-equilibrium effects dominate almost all gas bulk flow. The collisions between the gas molecules and wall surfaces are dominant and the intermolecular collisions can be ignored.

Table 5

Calculated density difference, Re and Ma numbers at all pressures applied during the experiments performed on the Eagle Ford shale sample.

Ave. Pore Pressure	Density Difference (%)	$Re = \frac{\rho_{ave} u_{int} d_p}{\mu}$	$Ma = Kn\,Re\sqrt{\frac{\gamma\pi}{2}}$
250	0.0042	8.71E-7	1.52E-7
750	0.0121	2.52E-6	1.51E-7
1500	0.0119	4.74E-6	1.48E-7
2250	0.0118	6.57E-6	1.45E-7
3000	0.0116	8.00E-6	1.41E-7

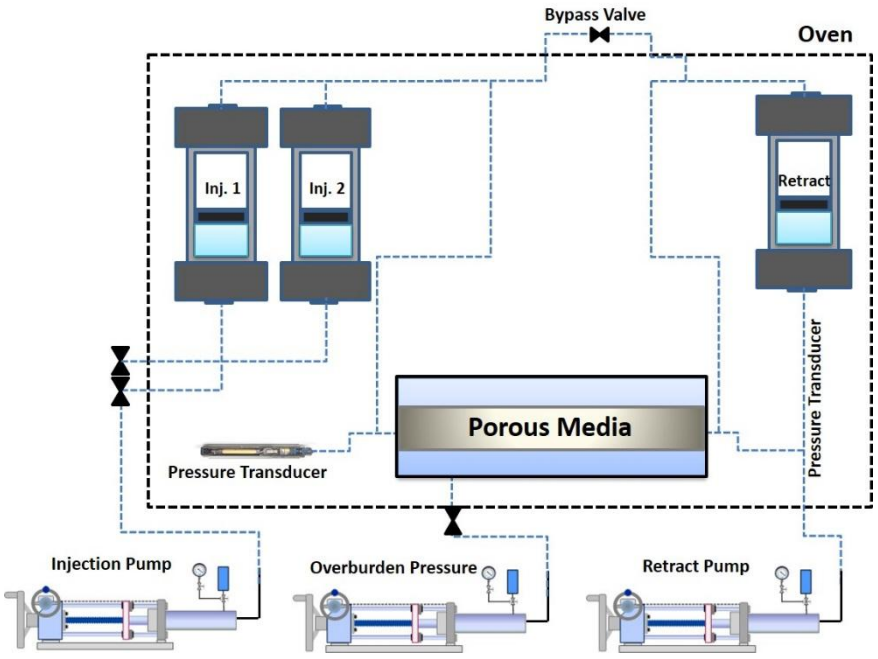

(a)

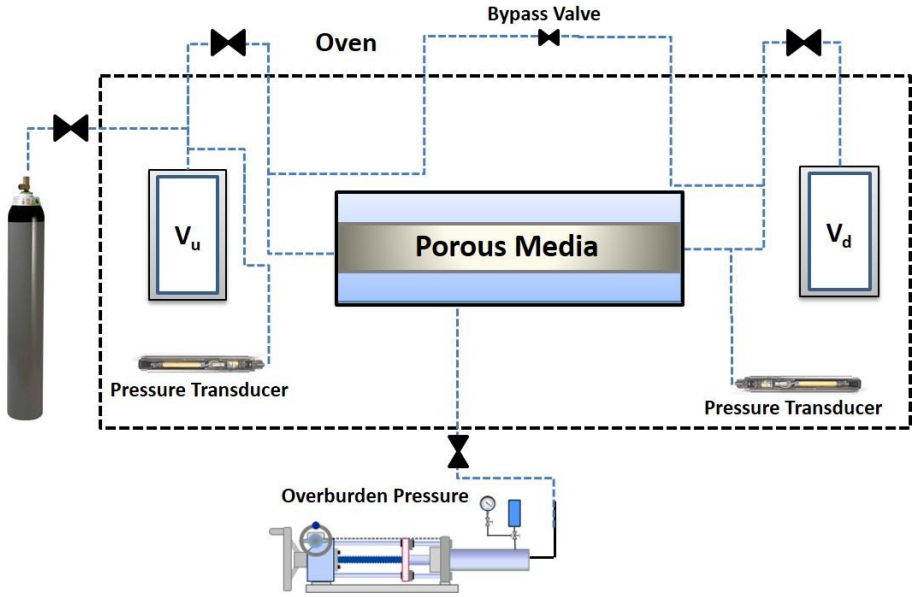

(b)

Fig. 5. The schematic diagram of (a) steady state and (b) unsteady state pulse-decay set up used here for the matrix permeability measurement.

3. Results and discussion

3.1. Apparent Matrix Permeability

Fig. 6 shows apparent permeability versus pore pressures at different net stress for three cores of Eagle Ford (Fig. 6a), Pierre (Fig. 6b) and Barnett Shale (Fig. 6c). As shown in these Figures, the apparent permeability is increased as the pore pressure decreased. This enhancement is higher at lower pore pressures as gas slippage is more dominant when Knudsen number is increased at lower pore pressures. The gas slippage is observed to happen in almost all cases, but to determine the slippage intensity, the non-slip permeability should be determined. From Fig. 6, it can be also concluded that the apparent permeability decreases as the net stress increases. In other words, the flow conduit size (pore size) is decreased by increasing the net stress. However, the resultant permeability reduction is not the same for all shale samples. In addition, it is found that the strength of gas slippage is different at different net stress.

Fig. 7, includes the same data as those noted in Fig. 6, but here the measured apparent permeabilities are plotted versus net stress. As shown in Fig. 7, almost all core samples are sensitive to the net stress such that the permeability can be decreased up to 10 times from 500

to 3000 psi net stress. This significant stress dependency of permeability is probably caused due to the presence of micro-fracture inside shale matrix. These micro-fractures, which have dominant contributions to flow, are more influenced by applied net stress compared to the other pore types (Kwon et al., 2004). However, it should be noted that the effect of stress on flow regime is not the same as its effect on matrix permeability. To study the effect of stress on flow regimes, the overall pore throat sizes should be considered, which can change the slippage intensity.

It is noted that the geo-mechanical effect on permeability is not the same at all net stresses, i.e. the permeability reduction is more severe at lower net stresses. It means that the matrix permeability is more sensitive to applied stress, when the pore pressure is close to overburden pressure (early time of production life). This sensitivity decreases gradually as the reservoir pore pressure decreases during the production period. In other words, as the pore pressure is reduced (higher Kn number), the slippage effect becomes more dominant and the geo-mechanical effects are less important. From Fig. 7, it is also noted that the stress effects on the matrix permeability is not the same for all shale rocks, i.e. it is more for higher permeability shale, Fig. 7(a).

Based on these results, it can be concluded that during the production life of a reservoir, both (i) permeability reduction due to geomechanical effects and (ii) permeability enhancement due to gas slippage occur simultaneously in shale/tight gas reservoirs due to pore pressure reduction caused by gas production. As these two mechanisms play important roles, in a competitive manner, quantification of their effects on matrix permeability is required for accurate prediction of matrix permeability.

In the following, first we obtain the non-slip permeability in each experiment and quantify the slippage effect based on the permeability enhancement factor, which is a dimensionless parameter ($K_{appr.}/K_{non-slip}$) at a given net stress. Then, the stress effects are taken into account by using a different average pore size.

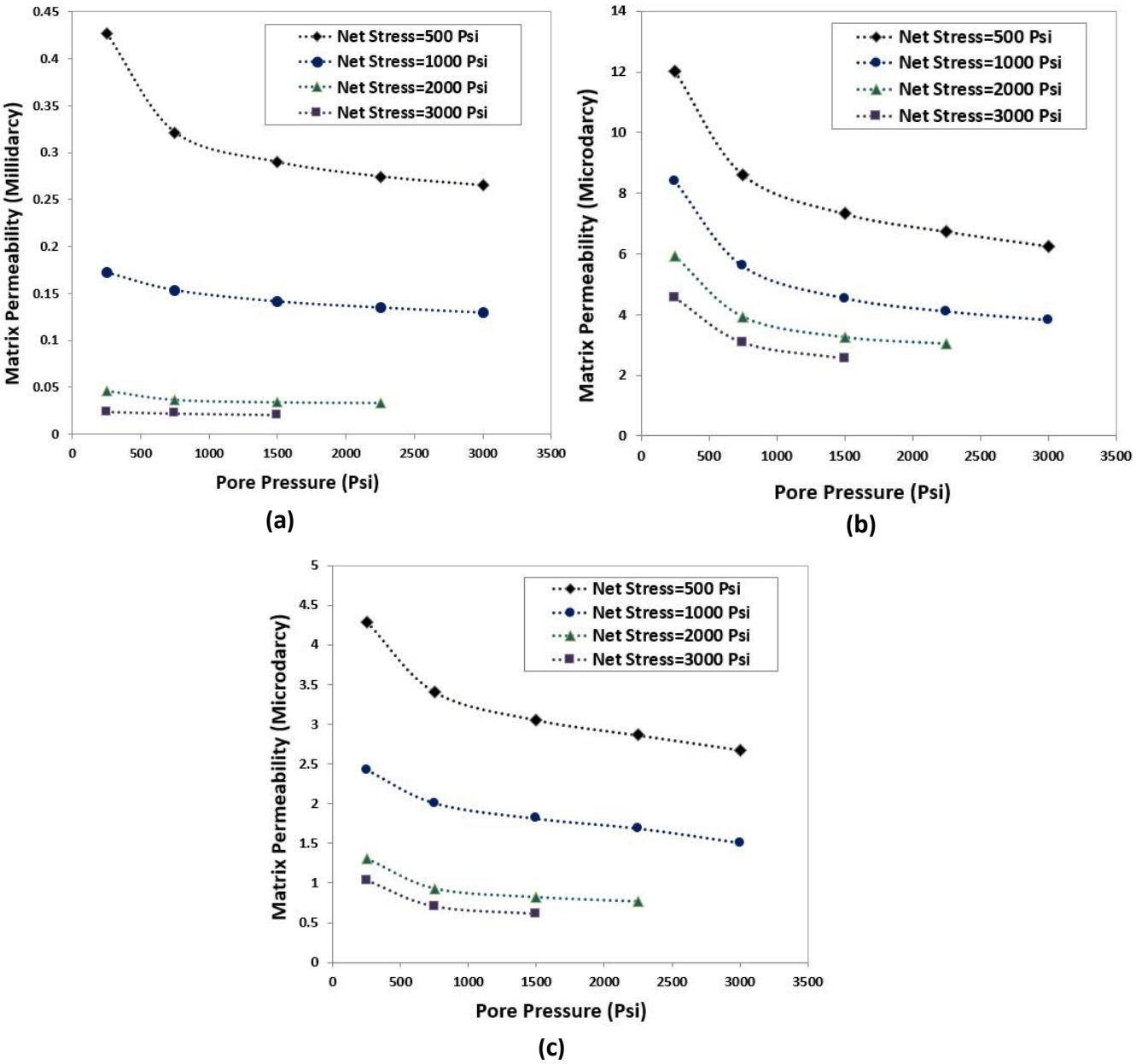

Figure 6: Measured apparent permeability versus pore pressure for (a) Eagle Ford, (b) Pierre and (c) Barnett shale cores at different net stresses.

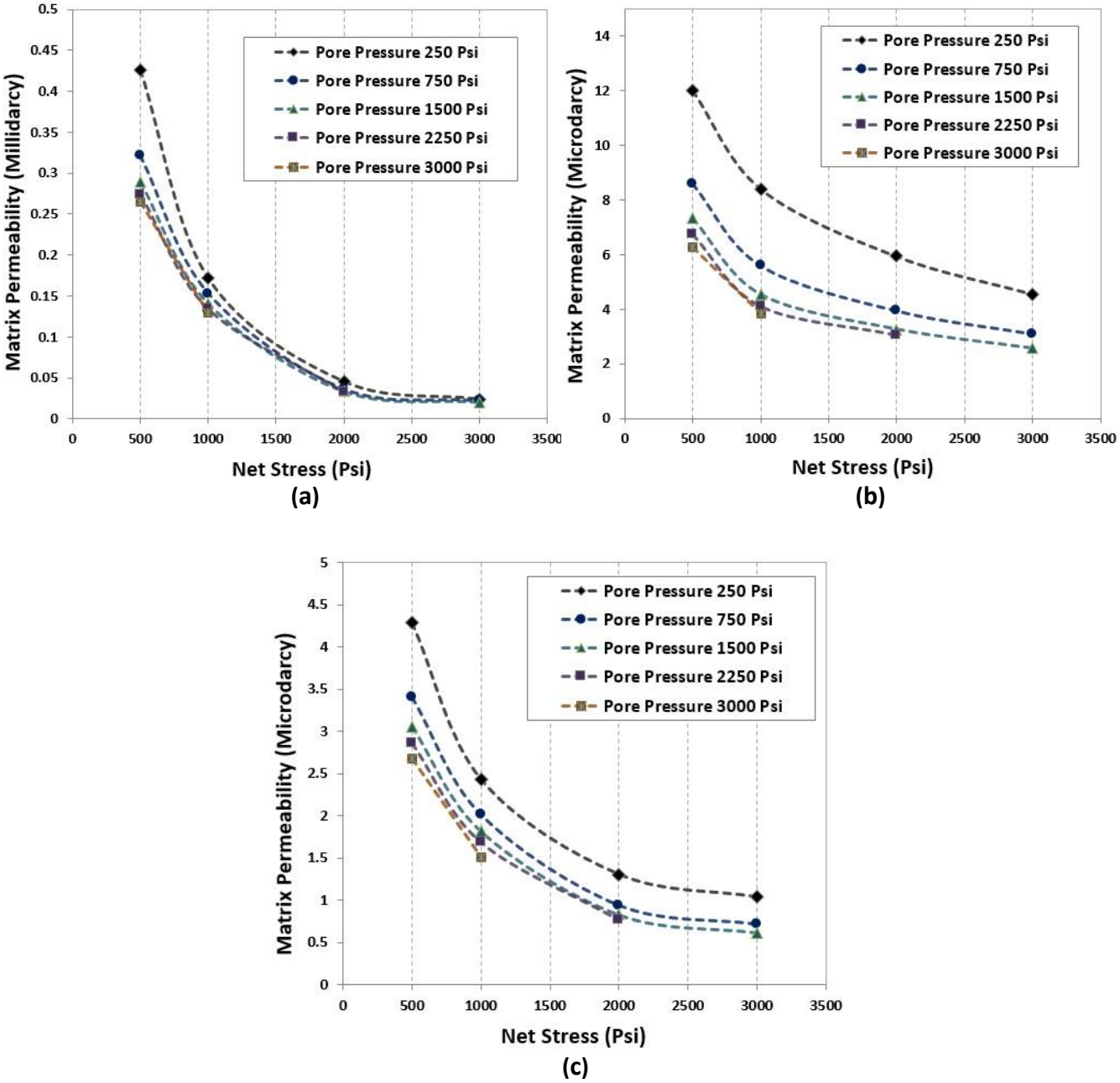

Figure 7: Measured apparent permeability versus net stress for (a) Eagle Ford, (b) Pierre and (c) Barnett shale cores at different pore pressures.

3.2. Non-slip Permeability Determination

Non-slip permeability, here is referred to as the absolute permeability of rock, when the slippage effect is not dominant. Based on the Klinkenberg correction, this permeability is equal to gas permeability at infinite gas pressure (Klinkenberg, 1941). Klinkenberg correction, which is a first-order slip model, gives a non-slip permeability based on the plot of the apparent permeability versus inverse pressure. In this study, non-slip permeabielies were predicted from the measured permeability at higher pressures (1500, 2250 and 3000 psi). The Klinkenberg correction method was used to find the permeability at infinite pressure by extrapolating the measured data. However, it was noted that the Klinkenberg correction approach deviates from the straight line, particularly for tighter cores at lower pressures, whereby the flow is in the transition regime. Hence, in this study, the non-slip permeability for each core sample was obtained by extrapolation of the measured permeabilities at pressure or above the 1500 psi (i.e. experimental data points with Kn < 0.1). It is evident that at higher pressures, the Knudsen number is low and the slip effects is minimal. Therefore extrapolation of these measured values probably gives an accurate non-slip permeability.

From the data of Fig. 8, corresponding to the net stress of 500 psi, the non-slip permeabilities are calculated as 0.240 md, 5.28 μd and 1.810 μd for Eagle ford, Pierre and Barnett shale rock samples, respectively. For other net stresses, the non-slip permeabilities have also been calculated using the same procedure with results shown in Table 6 and Fig. 9. As illustrated, the stress dependency of non-slip permeabilities follows an exponential relationship. The exponential constants of the best fitted lines in this study are close to those reported in the literature for the similar measurements (Chalmers et al., 2012b; Zhang et al., 2015). For example, Zhang et al (2015) performed similar measurements for eight shale samples and reported exponential constants varying from 0.05 to 0.12 which are in the range of values obtained here.

As described later, this relationship constitute part of our proposed procedure for incorporating the geo-mechanical effects into the slip model used for matrix permeability predictions.

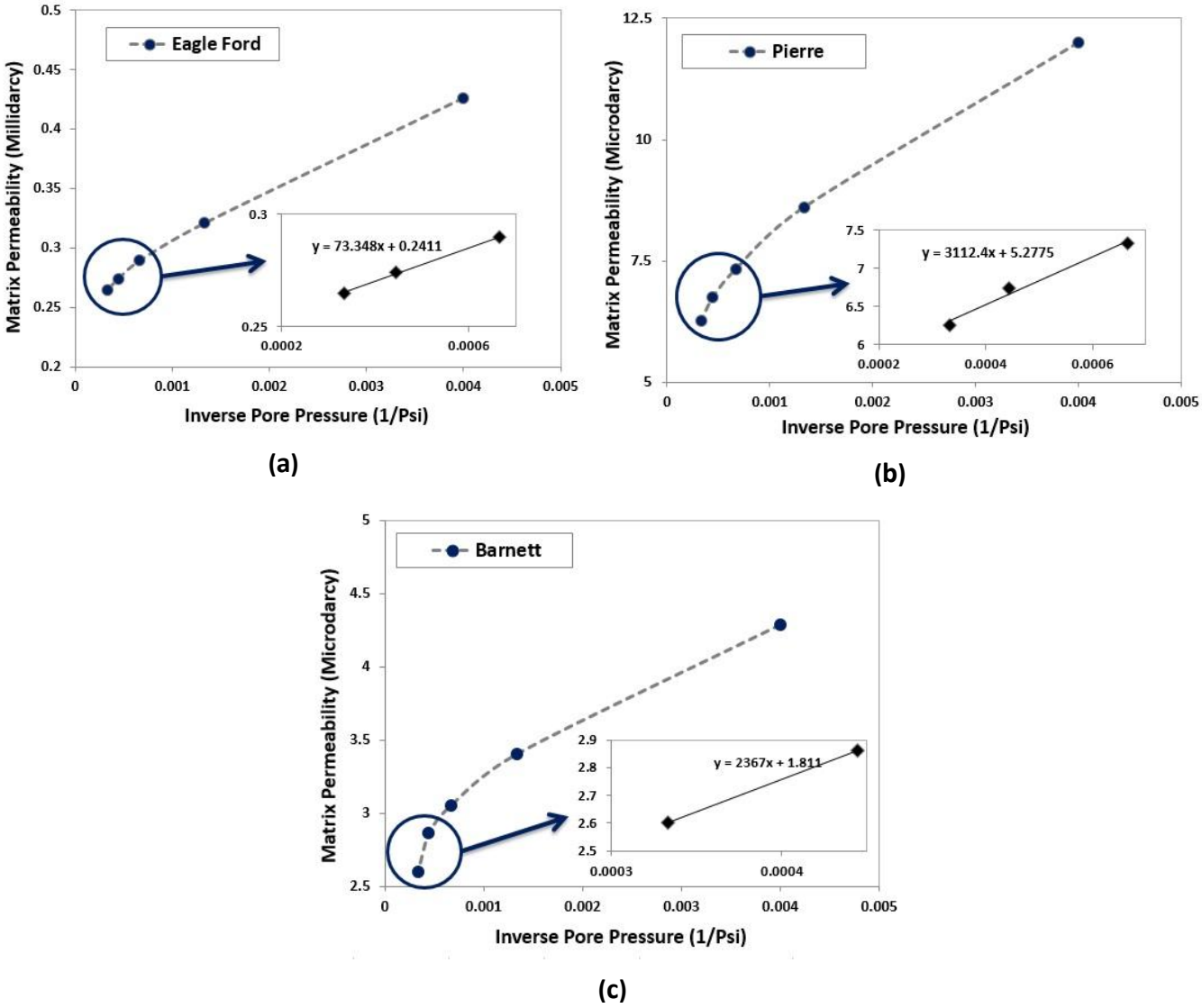

Fig. 8. Measured permeability versus inverse pore pressure (a) Eagle Ford, (b) Pierre and (c) Barnett shale core plugs at net stress of 500 psi. Measured permeability at high pressures (1500, 2250 and 3000 psi) are used for extrapolation to estimate non-slip permeability of each core plug; the lines connecting measured points are trend guides for the eye.

Table 6. The Klinkenberg corrected permeability (non-slip permeability) for three shale samples.

Net Stress (Psi)	Non-slip Matrix Permeability		
	Eagle Ford (mD)	Pierre (μD)	Barnett (μD)
500	0.240	5.28	1.81
1000	0.112	2.95	0.965
2000	0.026	2.10	0.450

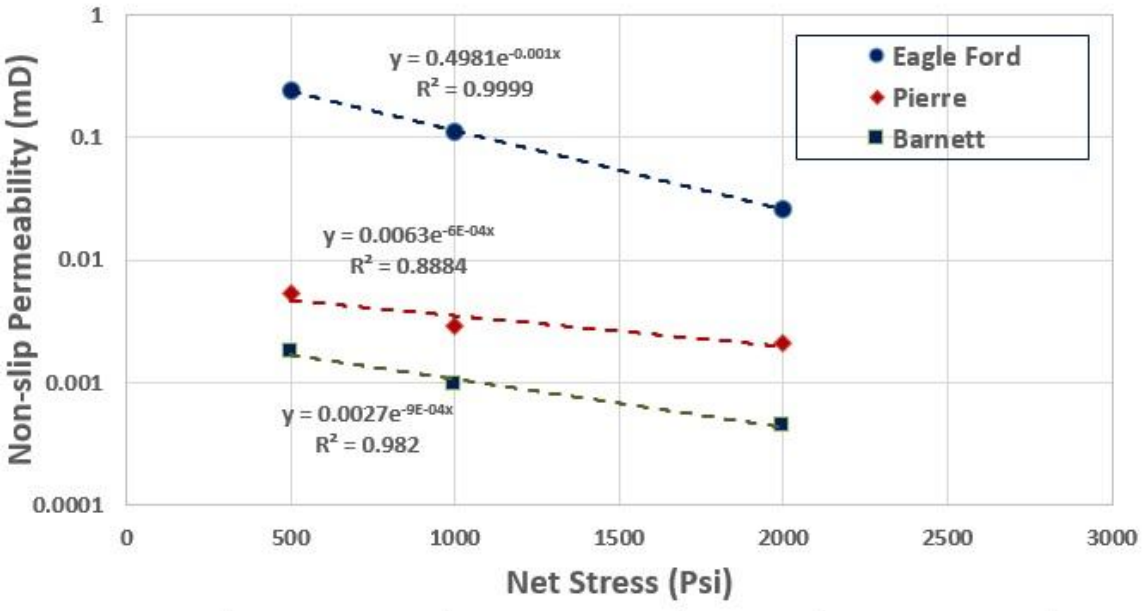

Figure 9. Non-slip permeability of three shale rock samples, calculated based on the Klinkenberg correction.

3.3. N-S Solution of Rarefied Flow: Slippage effect

The flow prediction of rarefied gas ($10^{-2} < Kn$) by Navier-Stokes equations is challenging due to the dominant role of Knudsen layer (KL). Inside the Knudsen layer, N-S equations are not able to capture the flow behaviour. It has been shown that the N-S

equations with slip boundary conditions can approximately predict the flow behaviour for the entire system in the slip regime. However the accuracy of this prediction decreases as the thickness of Knudsen layer increases (i.e. increasing Knudsen number). Among the slip boundary conditions, Maxwell slip model has been conventionally used to capture the rarefied flow. Based on his model, the first-order slip boundary condition can be written as follows (Here thermal creep effects have been neglected)

$$u_s - u_w = C\lambda \left(\frac{\partial u_s}{\partial n}\right)_s \quad (3)$$

Where u_w is the wall velocity, u_s is the slip velocity, n is the coordinate normal to the wall, C is slip coefficient and λ is gas mean free path. Later, and based on the Maxwell's theory, second-order boundary conditions have been proposed (Barber and Emerson, 2006; Dongari et al., 2007; Karniadakis et al., 2005). In general form, it can be written as:

$$u_s - u_w = C_1\lambda \left(\frac{\partial u_s}{\partial n}\right)_s + C_2\lambda^2 \left(\frac{\partial^2 u_s}{\partial n^2}\right)_s \quad (4)$$

where C_1 and C_2 are the first and second order slip coefficients, respectively. Using the general second-order slip boundary condition and assuming a bundle of capillary tubes for porous media, the following equation can be obtained for the apparent permeability.

$$K_D = \frac{k_{app}}{k_{non-slip}} = [1 + 4C_1Kn - 8C_2Kn^2] \quad (5)$$

Therefore based on the second-order slip models, the dimensionless permeability can be plotted versus Knudsen number. In Fig. 10, the dimensionless permeability factor, K_D, is calculated for each experiment and plotted versus Knudsen number. As mentioned, the experimental results can be used to find the first and second order slip coefficients, i.e. C_1 and C_2 by fitting Equation 5 using the least squared method. Following this procedure, 2.390 and 2.392 values were obtained for C_1 and C_2, respectively. More details about the slip models and their link in the N-S solution of rarefied flow in porous media can be found elsewhere (Nazari Moghaddam and Jamiolahmady, 2016).

It should be noted that all the data points in Fig. 10 follows the same trend confirming that the dimensionless permeability can be plotted versus Knudsen number regardless of rock type and flowing gas type. In other words, because other petrophysical properties of flow conduits are the same when obtaining K_{appr} and $K_{non\text{-}slip}$., a plot is obtained, which is independent of the rock type. From such a plot, one can predict the apparent matrix permeability at known dimensionless Knudsen number. These results are in good agreement with literature data

published recently for apparent matrix permeability in different porous media (Heller et al., 2014; Sinha et al., 2013; Yves et al., 2015).

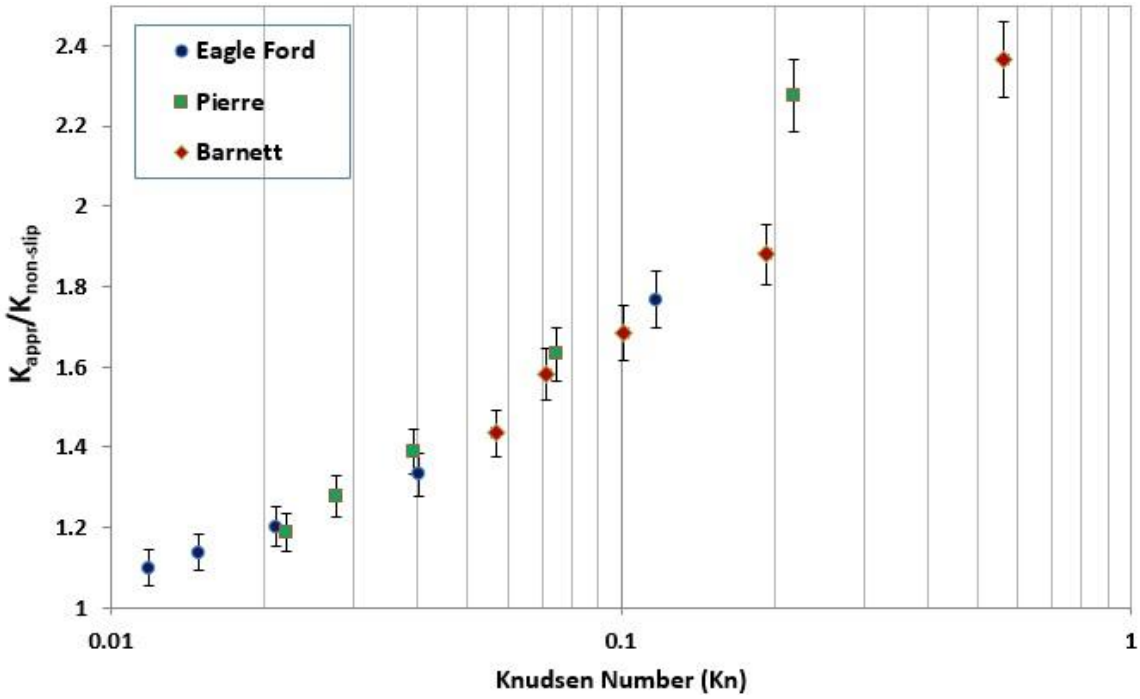

Fig. 10. Dimensionless permeability factor versus Knudsen number for three shale rock samples at constant net stress of 500 psi.

3.4. N-S Solution of Rarefied Flow: Stress effect

As mentioned earlier, during the production life, reservoir pore pressure decreases and overall net stress increases. This net stress enhancement causes the matrix permeability to reduce. This effect is more pronounced in shale reservoirs due to higher sensitivity of these rocks to stress. Moreover in these reservoirs, the slippage phenomenon, which also plays an important role on the permeability and varies with pressure, makes the permeability prediction more difficult.

In order to consider the stress effects on apparent matrix permeability, N-S equations solved by the slip boundary models, described above in Equation 5, can be used. It should be noted that the pore size distribution changes as the net stress varies during the production period. In other words, the characteristic length of the flow should be modified as a result of changing the applied net stress. In addition, as a result of a change in net stress, the non-slip permeability also varies. Several authors have shown that the non-slip permeability decreases

as the net stress increases.(Chalmers et al., 2012b; Ghanizadeh et al., 2014b; Heller et al., 2014). Considering the above discussion, it is reasonable to propose that two parameters of "characteristic length" and "non-slip permeability" should be modified to capture the stress effect on the matrix permeability.

In this study, the experimental data performed at 1000 and 2000 net stress are used to investigate the geo-mechanical effects (The number of permeability data points measured at 3000 psi net stress was not sufficient to be included in this investigation). To quantify these effects, characteristic length and non-slip permeability of porous media should be determined at each net stress. As explained before, the non-slip permeability of shale samples were calculated based on the Klinkenberg correction applied to the experimental data performed at high pressures (1500, 2250 and 3000 psi) as shown in Table 6 and Fig. 9. As illustrated in this Figure, the non-slip permeability follows an exponential relationship. This exponential behaviour can be used in the slip model (Equation 5) to predict the apparent permeability.

Another factor which should be modified by changing net stress is the average pore size, i.e. characteristic length of flow conduit. In order to find the fluid flow characteristic length, the generalized slip plot (Fig. 10) was used. As mentioned, the general slip plot shown in Fig. 10 was generated based on the permeability data measured at 500 psi net stress. At higher net stresses the dimensionless permeabilities are calculated based on the measured apparent permeability and estimated non-slip permeability of the rock. Then the characteristic length of the flow (for calculation of Knudsen number) is changed to find the best match on Fig. 10. In other words, the average pore size of the flow conduit is determined based on the tuning process. Fig. 11, is similar to Fig. 10, but also includes the data measured on these three rocks at a net stress of 1000 psi. As seen in this figure, all the data points follow the same trend as that shown in the generalized slip plot of Fig. 10. This suggests that the stress effect can be quantified using an appropriate average pore size. It is noted that when the permeability data measured at 2000 psi net stress are placed at the same graph (Fig. 12), all data points measured at different net stresses obey the same trend provided that the characteristic length of the porous media are determined appropriately.

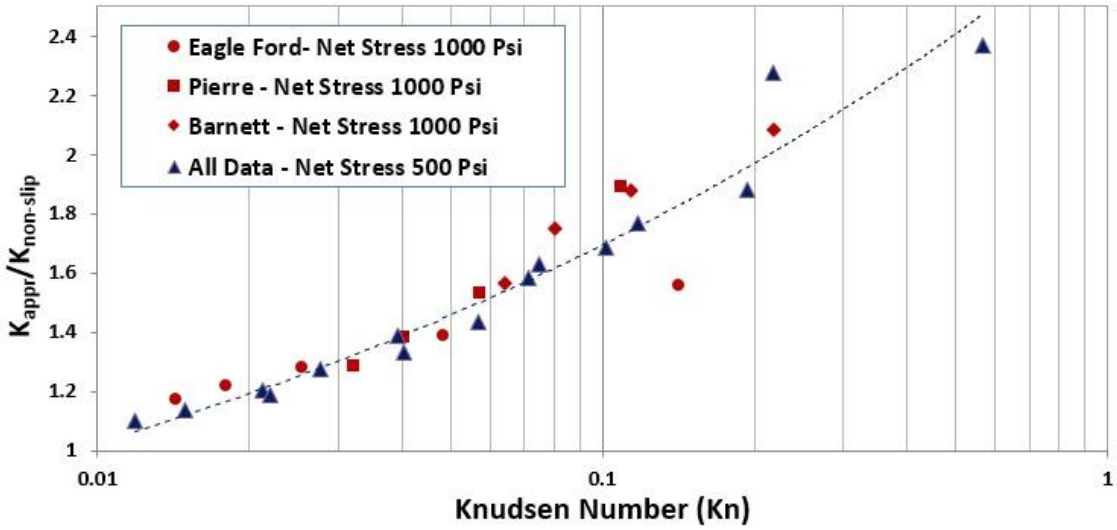

Fig. 11. Dimensionless permeability factor versus Knudsen number for three shale rock samples at constant net stress of 500 and 1000 psi; the permeability factors measured at 1000 psi net stress follow the generalized slip plot shown in Figure 10.

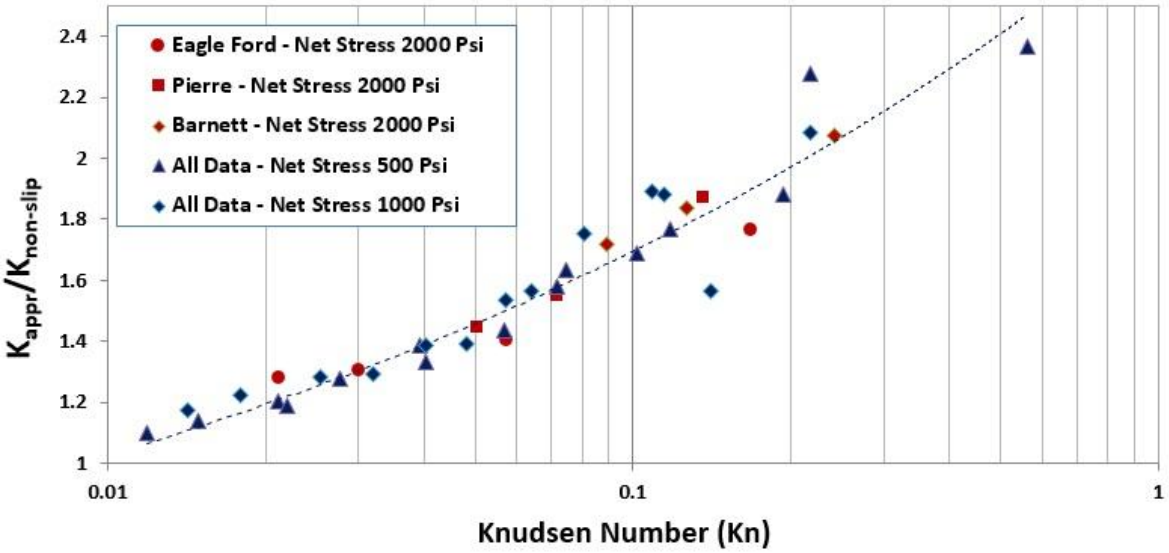

Fig. 12. Dimensionless permeability factor versus Knudsen number for three shale rock samples at constant net stress of 500, 1000 and 2000 psi; the permeability factors measured at both 2000 and 1000 psi net stresses follow the generalized slip plot shown in Fig. 10.

Table 7 presents the allocated average pore size at different net stresses. As indicated, the average pore size decreases as the net stress increases. The obtained average size are plotted versus net stress in Fig. 13. The average pore size decreases by increasing the net stress, following an exponential relationship.

As mentioned earlier, the measured MICP data were fitted by a probability distribution functions to find the pore size statistical parameters (Table 3). In Fig. 14, the obtained average pore sizes (mean) at different net stress are used in those fitted functions to plot the pore size distribution. As illustrated in this Figure, the pore size distribution plot shifts to the left as the net stress decreases. For generation of these plots, it is assumed that geo-mechanical stress affects all pores uniformly.

Table 7. The obtained average pore size of shale samples at different net stresses; these data are used as characteristic lengths for calculation of Knudsen number.

Net Stress (Psi)	Average Characteristic Length (nm)		
	Eagle Ford	Pierre	Barnett
500	54	29.1	11.25
1000	45	20	10
2000	38	16	9

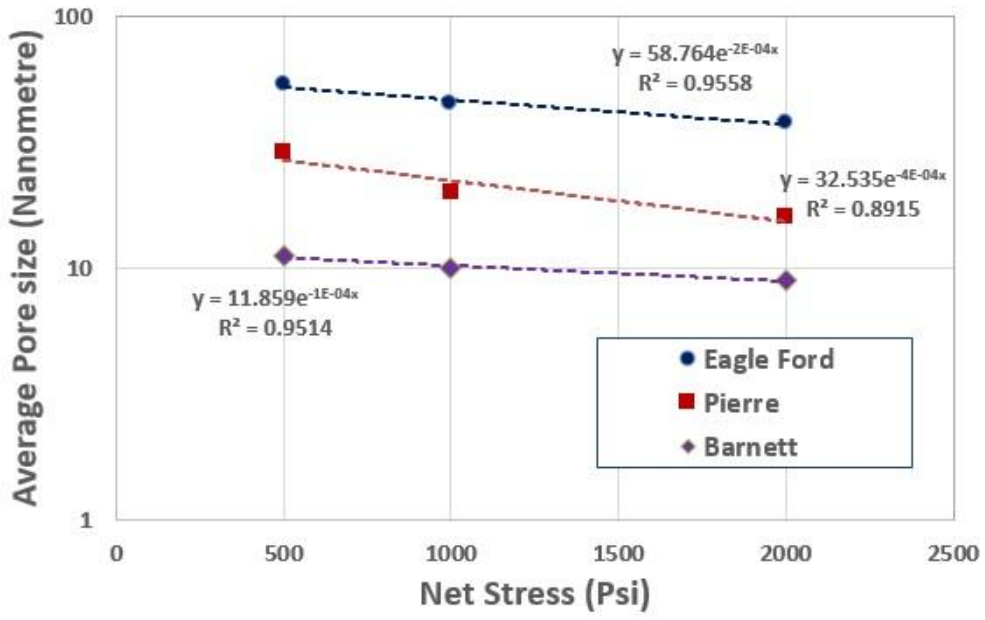

Fig. 13. Data of average pore size of three shale rock samples at three different net stress obtained through the introduced matching process.

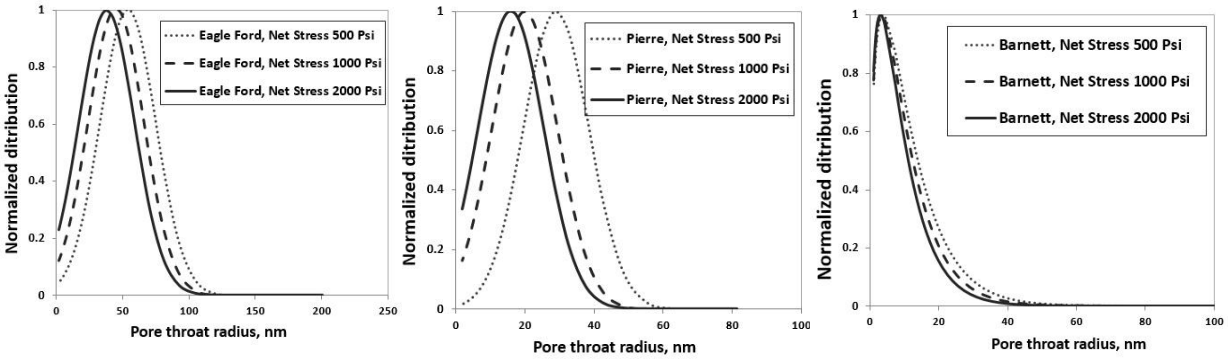

Fig. 14. The pore size distribution of three shale rock samples at three different net stress. The average pore size of shale sample at any net stress was used in the corresponding appropriate probability distribution function.

In summary based on the experimental observations in this study, it is proposed to predict the apparent matrix permeability as a function of net stress assuming two separate exponential relationships for reduction of both non-slip permeability and average pore size. In other words, the slippage can be considered in the flow equations by assuming slip boundary conditions (first or second order slip model) and the stress effect can be taken into account in the same equation by assuming two exponential relationships for non-slip permeability and average pore size. Hence, the final solution has the following form:

$$k_{app} = k_{non-slip}\left[1 + 4C_1\left(\frac{\lambda}{R_c}\right) - 8C_2\left(\frac{\lambda}{R_c}\right)^2\right] \quad (6)$$

where

$$k_{non-slip} = {k^0}_{non-slip}[\exp\left(\alpha \times \Delta P\right)] \quad (7)$$

$$R_c = {R^0}_c[\exp\left(\beta \times \Delta P\right)] \quad (8)$$

where ${k^0}_{non-slip}$ and ${R^0}_c$ are the non-slip permeability and characteristic radius (average pore radius) at a reference net stress, α and β are fitting parameters, C_1 and C_2 are first and second order slip coefficients, respectively and ΔP is the net stress difference from the reference pressure. It is noted that the base non-slip permeability (${k^0}_{non-slip}$) can be assumed as absolute or intrinsic permeability as it is independent of both slippage and net stress. Therefore to predict the apparent matrix permeability of a rock, the base non-slip permeability (${k^0}_{non-slip}$) and average pore size (${R^0}_c$) should be measured in the laboratory. In addition, the exponential parameters (α and β in Equations 7 and 8) are required which

can be calculated from few permeability measurements at different pore pressure and net stress.

It has to be reminded that the slippage intensity is a function of Knudsen number. Hence, slippage is more pronounced, when the Knudsen number is high, i.e. the size of flow conduit is small. Therefore, larger flow conduits have less impact on the flow in terms of slippage. While larger conduits have greater effects on flow in terms of rock permeability. In other words, in this model, the "permeability reduction" is separated from the "characteristic size reduction" and the introduced fitting coefficients capture these dependencies that would change from rock to rock depending on the pore type, minerology, pore size distribution and etc. Knowing these basic data, the permeability at any net stress and pore pressure can be estimated, based on the proposed model, and used for simulation of gas flow in matrix during the reservoir life.

3.5. Model Verification

In this section, the validity of the proposed model is examined. To achieve this aim, series of experimental data were sourced from the literature. Ghanizadeh et al. (2014) reported several matrix permeability measurements on the Scandinavian Alum Shale (Ghanizadeh et al., 2014b). They investigated the effects of different pertinent parameters including moisture content, permeating fluid, effective stress, and pore pressure. In this work, we used the measured apparent permeability data reported for Alum#2.

Some of reported data points at different pore pressure and net stress were used to obtain the base ${k^0}_{non-slip}$ and α parameters in Equation 7 and ${R^0}_c$ and β parameters in Equation 8. The obtained ${k^0}_{non-slip}$, α, ${R^0}_c$ and β values are 52, -2.5E-4, 136.2 and -6.2E-4, respectively. For calculation of these parameters, the non-slip permeabilities were estimated using the Klinkenberg correction. Then the non-slip permeability data were plotted versus net stress to obtain the parameters of Equation 7. The non-slip permeability data showed a good exponential trend similar to what have been reported here for three shale samples used in our experiments. Next, the average pore size data were calculated at each net stress following the matching process, which was described in Section 3.4 and using the apparent permeability data measured at three pore pressures. It is noted that the average size data for Alum#2 also showed a good exponential trend. Having the non-slip permeability (${k^0}_{non-slip}$ and α) and average pore size (${R^0}_c$ and β) parameters, the apparent permeability at other pore pressure and net stress were estimated using Equations 6, 7 and 8. Fig. 15 shows the predicted values

of apparent matrix permeability at different pore pressures and net stresses. As shown in this Figure, the proposed model can capture both permeability enhancement and reduction due to slippage and stress, respectively. It should be noted that these data points were not used for obtaining the parameters in Equation 7 and 8. Table 8 indicates the corresponding pore pressure and net stress in each experiment. The corresponding error for each prediction is also shown in this Table.

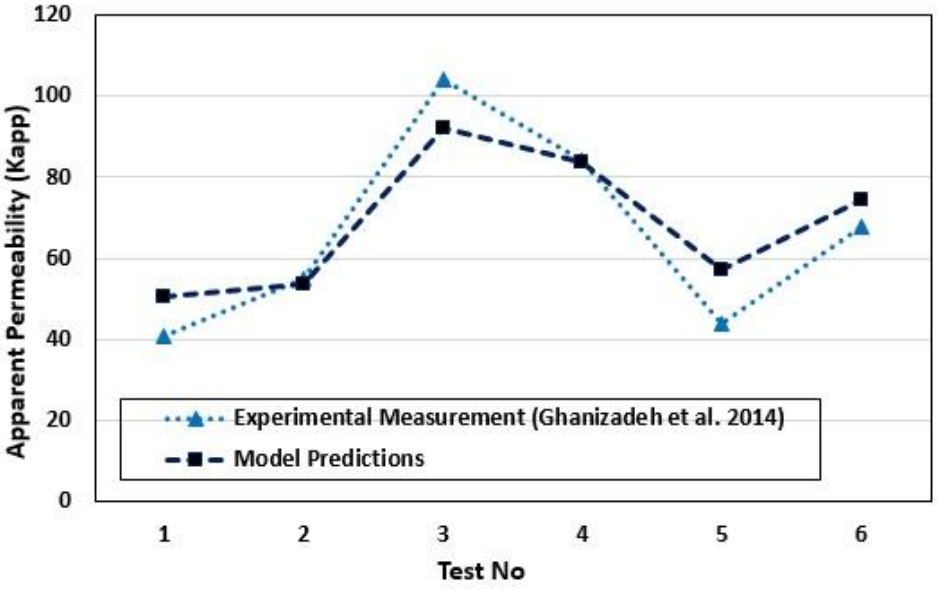

Fig. 15. Comparison of predicted apparent permeability data of the Alum#2 shale rock sample with the corresponding experimental data reported by Ghanizadeh et al.(2014).

Table 8. The predicted apparent permeability data for the Alum#2 shale sample. The predicted values are compared with the corresponding experimental data reported by Ghanizadeh et al. (2014).

Test No	Pore Pressure (Psi)	Net Stress (Psi)	Measured Permeability (nD)	Predicted Permeability (nD)	Error %	Kn Number
1	464	3146	41	50.6	23.4	0.15
2	464	1290	55	53.7	2.3	0.05
3	101.5	1058	104	92.1	11.4	0.18
4	101.5	2088	84	83.8	0.3	0.35
5	319	3306	44	57.3	30.2	0.24
6	174	1566	68	74.5	9.5	0.15

4. Summary and conclusion

In this study, the effects of geo-mechanical and slip flow were studied. Series of experiments were designed and performed on three shale samples to measure apparent matrix permeabilities at five different pore pressure and four net stress values. Steady state and unsteady state techniques were used to measure the gas permeability. For Knudsen number calculation, the average pore size of each shale rock sample was determined using the experimentally measured Mercury injection capillary pressure (MICP) data. The Klinkenberg correction was used to find the non-slip permeability at infinite pressure by extrapolating the trend of measured data at high pressures in the plot of apparent permeability versus inverse of pressure. The obtained non-slip permeability data were used to calculate the permeability enhancement factor, which is a dimensionless parameter. The obtained dimensionless permeability ratio data at various Knudsen numbers were used to generate a general slip plot, which is independent of rock and fluid properties. The impact of net stress on permeability was accounted based on the reduced average pore size (for calculation of Knudsen number) and non-slip permeability. The following observations/conclusions can be made/drawn from this study:

- At any given net stress, the matrix permeability increased as pressure decreased due to gas slippage at the pore walls. At any pore pressure, the matrix permeability decreased as the net stress increased in all experiments.
- The shale matrix permeability was more sensitive to the applied stress, when the pore pressure was close to the overburden pressure. This sensitivity decreased gradually as the reservoir pore pressure decreased.
- Solution of the Navier-Stokes equation, using the second order Maxwell's slip boundary condition, gave the first and second-order slip coefficients of 2.390 and 2.392, respectively.
- The stress dependency of non-slip permeabilities followed an exponential relationship. The power exponents of the best fitted lines are in good agreement with those reported in the literature data.
- The corresponding reduced average pore size at higher net stress was obtained by matching the corresponding data to the trend of the generalised plot. These data also followed an exponential relationship.
- These two functions, together with the solution of Navier-Stokes equation were used to verify the reliability of the proposed method using the literature data showing that the

proposed model could capture both permeability enhancement and reduction due to slippage and stress, respectively, with reasonable accuracy.

The outcomes of this study increases our knowledge of the impact of geomechanical stress on rarefied gas flow in tight and shale gas reservoirs. Based on the results, the apparent matrix permeability can be better predicted considering both slippage and geomechanical effects using the available slip coefficients and following the proposed techniques for modifying the average pore size and non-slip permeability. However, the current paper presents experimental data performed on three specific shale samples, hence, more investigations are demanded to improve the findings.

Acknowledgements

This study was conducted as a part of the Unconventional Gas and Gas-condensate Recovery Project at Heriot-Watt University. This research project is sponsored by: Daikin, Dong Energy, Ecopetrol/Equion, ExxonMobil, GDF, INPEX, JX-Nippon, Petrobras, RWE, Saudi-Aramco and TOTAL, whose contribution is gratefully acknowledged.

References

Barber, R.W., Emerson, D.R., 2006. Challenges in modeling gas-phase flow in microchannels: from slip to transition. Heat Transfer Engineering 27, 3-12.

Bourbie, T., Walls, J., 1982. Pulse Decay Permeability: Analytical Solution and Experimental Test. Society of Petroleum Engineers Journal 55.

Brace, W.F., Walsh, J., Frangos, W., 1968. Permeability of granite under high pressure. Journal of Geophysical research 73, 2225-2236.

Bustin, A.M., Bustin, R.M., 2012. Importance of rock properties on the producibility of gas shales. International Journal of Coal Geology 103, 132-147.

Bustin, A.M., Bustin, R.M., Cui, X., 2008. Importance of fabric on the production of gas shales, SPE Unconventional Reservoirs Conference. Society of Petroleum Engineers.

Chalmers, G.R., Bustin, R.M., Power, I.M., 2012a. Characterization of gas shale pore systems by porosimetry, pycnometry, surface area, and field emission scanning electron microscopy/transmission electron microscopy image analyses: Examples from the Barnett, Woodford, Haynesville, Marcellus, and Doig units. AAPG bulletin 96, 1099-1119.

Chalmers, G.R., Ross, D.J., Bustin, R.M., 2012b. Geological controls on matrix permeability of Devonian Gas Shales in the Horn River and Liard basins, northeastern British Columbia, Canada. International Journal of Coal Geology 103, 120-131.

Chen, T., Stagg, P.W., 1984. Semilog Analysis of the Pulse-Decay Technique of Permeability Measurement. Society of Petroleum Engineers Journal 24.

Civan, F., 2010. Effective correlation of apparent gas permeability in tight porous media. Transport in porous media 82, 375-384.

Cui, X., Bustin, A., Bustin, R.M., 2009. Measurements of gas permeability and diffusivity of tight reservoir rocks: different approaches and their applications. Geofluids 9, 208-223.
Darabi, H., Ettehad, A., Javadpour, F., Sepehrnoori, K., 2012. Gas flow in ultra-tight shale strata. Journal of Fluid Mechanics 710, 641-658.
Deng, J., Zhu, W., Ma, Q., 2014. A new seepage model for shale gas reservoir and productivity analysis of fractured well. Fuel 124, 232-240.
Dewhurst, D.N., Siggins, A.F., 2006. Impact of fabric, microcracks and stress field on shale anisotropy. Geophysical Journal International 165, 135-148.
Dicker, A.I., Smits, R.M., 1988. A Practical Approach for Determining Permeability From Laboratory Pressure-Pulse Decay Measurements, International Meeting on Petroleum Engineering. Society of Petroleum Engineers, Tianjin, China.
Dong, J.-J., Hsu, J.-Y., Wu, W.-J., Shimamoto, T., Hung, J.-H., Yeh, E.-C., Wu, Y.-H., Sone, H., 2010. Stress-dependence of the permeability and porosity of sandstone and shale from TCDP Hole-A. International Journal of Rock Mechanics and Mining Sciences 47, 1141-1157.
Dongari, N., Agrawal, A., Agrawal, A., 2007. Analytical solution of gaseous slip flow in long microchannels. International Journal of Heat and Mass Transfer 50, 3411-3421.
Evans, J.P., Forster, C.B., Goddard, J.V., 1997. Permeability of fault-related rocks, and implications for hydraulic structure of fault zones. Journal of Structural Geology 19, 1393-1404.
Fathi, E., Akkutlu, I.Y., 2013. Lattice Boltzmann Method for Simulation of Shale Gas Transport in Kerogen. Society of Petroleum Engineers Journal 18.
Firouzi, M., Alnoaimi, K., Kovscek, A., Wilcox, J., 2014. Klinkenberg effect on predicting and measuring helium permeability in gas shales. International Journal of Coal Geology 123, 62-68.
Florence, F.A., Rushing, J., Newsham, K.E., Blasingame, T.A., 2007. Improved Permeability Prediction Relations for Low Permeability Sands, Rocky Mountain Oil & Gas Technology Symposium. Society of Petroleum Engineers, Denver, Colorado, U.S.A.
Freeman, C., Moridis, G., Blasingame, T., 2011. A numerical study of microscale flow behavior in tight gas and shale gas reservoir systems. Transport in porous media 90, 253-268.
Ghanizadeh, A., Amann-Hildenbrand, A., Gasparik, M., Gensterblum, Y., Krooss, B.M., Littke, R., 2014a. Experimental study of fluid transport processes in the matrix system of the European organic-rich shales: II. Posidonia Shale (Lower Toarcian, northern Germany). International Journal of Coal Geology 123, 20-33.
Ghanizadeh, A., Gasparik, M., Amann-Hildenbrand, A., Gensterblum, Y., Krooss, B.M., 2014b. Experimental study of fluid transport processes in the matrix system of the European organic-rich shales: I. Scandinavian Alum Shale. Marine and Petroleum Geology 51, 79-99.
Gutierrez, M., Katsuki, D., Tutuncu, A., 2014. Determination of the continuous stress-dependent permeability, compressibility and poroelasticity of shale. Marine and Petroleum Geology.
Gutierrez, M., Øino, L., Nygård, R., 2000. Stress-dependent permeability of a de-mineralised fracture in shale. Marine and Petroleum Geology 17, 895-907.
Heller, R., Vermylen, J., Zoback, M., 2014. Experimental investigation of matrix permeability of gas shales. AAPG bulletin 98, 975-995.
Hildebrand, J., 1976. Viscosity of dilute gases and vapors. Proceedings of the National Academy of Sciences 73, 4302-4303.
Hsieh, P., Tracy, J., Neuzil, C., Bredehoeft, J., Silliman, S., 1981. A transient laboratory method for determining the hydraulic properties of 'tight'rocks—I. Theory, International Journal of Rock Mechanics and Mining Sciences & Geomechanics Abstracts. Elsevier, pp. 245-252.
Javadpour, F., 2009. Nanopores and Apparent Permeability of Gas Flow in Mudrocks (Shales and Siltstone). J Can Petrol Technol 48.
Jennings, D.S., Antia, J., Camp, W., Diaz, E., Wawak, B., 2013. Petrographic characterization of the Eagle Ford Shale, South Texas: Mineralogy, common constituents, and distribution of nanometer-scale pore types. Electron microscopy of shale hydrocarbon reservoirs: AAPG Memoir 102, 101-114.

Jones, F.O., Owens, W., 1980. A laboratory study of low-permeability gas sands. Journal of Petroleum Technology 32, 1,631-631,640.
Jones, S., 1997. A technique for faster pulse-decay permeability measurements in tight rocks. SPE Formation Evaluation, 19-26.
Kalantari-Dahaghi, A., 2011. Systematic approach to numerical simulation and modelling of shale gas reservoirs. International Journal of Oil, Gas and Coal Technology 4, 209-243.
Karniadakis, G., Beskok, A., Aluru, N., 2005. Microflows and nanoflows: fundamentals and simulation. Springer Science & Business Media.
Kazemi, M., Takbiri-Borujeni, A., 2015. An analytical model for shale gas permeability. International Journal of Coal Geology 146, 188-197.
Klinkenberg, L.J., 1941. The Permeability Of Porous Media To Liquids And Gases. American Petroleum Institute.
Kwon, O., Kronenberg, A.K., Gangi, A.F., Johnson, B., Herbert, B.E., 2004. Permeability of illite-bearing shale: 1. Anisotropy and effects of clay content and loading. Journal of Geophysical Research: Solid Earth (1978–2012) 109.
Loucks, R., Reed, R., Ruppel, S., Hammes, U., 2010. Preliminary classification of matrix pores in mudrocks: Gulf Coast Association of Geological Societies Transactions, v. 60. ndash 441, 435.
Nazari Moghaddam, R., Jamiolahmady, M., 2016. Slip flow in porous media. Fuel 173, 298-310.
NIST, 2015. National Institute of Standards and Technology. http://webbook.nist.gov/chemistry/fluid/.
Schmoker, J.W., Halley, R.B., 1982. Carbonate porosity versus depth: a predictable relation for south Florida. AAPG Bulletin 66, 2561-2570.
Sinha, S., Braun, E., Determan, M., Passey, Q., Leonardi, S., Boros, J., Wood III, A., Zirkle, T., Kudva, R., 2013. Steady-state permeability measurements on intact shale samples at reservoir conditions-effect of stress, temperature, pressure, and type of gas, SPE Middle East Oil and Gas Show and Conference. Society of Petroleum Engineers.
Swami, V., Settari, A., 2012. A pore scale gas flow model for shale gas reservoir, SPE Americas Unconventional Resources Conference. Society of Petroleum Engineers.
Wu, K., Li, X., Wang, C., Chen, Z., Yu, W., 2015. A model for gas transport in microfractures of shale and tight gas reservoirs. AIChE Journal 61, 2079-2088.
Yves, G., Amin, G., Robert, C.J., Amann-Hildenbrand, A., Krooss, B.M., Clarkson, C.R., Harrington, J.F., Zoback, M.D., 2015. Gas storage capacity and transport in shale gas reservoirs–A review. Part A: Transport processes. Journal of Unconventional Oil and Gas Resources.
Zhang, R., Ning, Z., Yang, F., Wang, X., Zhao, H., Wang, Q., 2015. Impacts of nanopore structure and elastic properties on stress-dependent permeability of gas shales. Journal of Natural Gas Science and Engineering.
Zhang, W.-M., Meng, G., Wei, X., 2012. A review on slip models for gas microflows. Microfluidics and nanofluidics 13, 845-882.